Fabrication and analysis of cylindrical resin AFM microcantilevers

Journal Item

Ultramicroscopy ▮ (▮▮▮▮) ▮▮▮–▮▮▮

Contents lists available at ScienceDirect

Ultramicroscopy

journal homepage: www.elsevier.com/locate/ultramic

Fabrication and analysis of cylindrical resin AFM microcantilevers

D. Cheneler [a,*], J. Bowen [b], S.J. Leigh [c], C.P. Purssell [c], D.R. Billson [c], D.A. Hutchins [c], M.C.L. Ward [a]

[a] School of Mechanical Engineering, The University of Birmingham, Edgbaston, Birmingham B15 2TT, UK
[b] School of Chemical Engineering, The University of Birmingham, Edgbaston, Birmingham B15 2TT, UK
[c] School of Engineering, University of Warwick, Coventry CV4 7AL, UK

ARTICLE INFO

Article history:
Received 12 December 2010
Received in revised form
25 February 2011
Accepted 11 March 2011

Keywords:
Atomic force microscope
Cantilever
Direct Digital Manufacturing
Timoshenko
Indentation

ABSTRACT

In this paper a new method of fabricating cylindrical resin microcantilevers using the Direct Digital Manufacturing (DDM) technique of Micro-stereolithography (MSL) is described. The method is rapid and commercially viable, allowing the fabrication of atomic force microscope (AFM) cantilevers which exhibit much larger spring constants than those currently commercial available. This allows for experimentation in a force regime orders of magnitude higher than currently possible using the AFM. This makes these cantilevers ideally suited for AFM-based depth sensing indentation. Due to their geometry, the assumptions used in the standard Euler–Bernoulli beam theory usually used to analyse AFM cantilevers may no longer be valid. Therefore approximate analytical solutions based on Timoshenko beam theory have been derived for the stiffness and resonant frequency of these cantilevers. Prototypes of the cantilevers have been fabricated and tested. Results show good agreement between experiment and theory.

1. Introduction

The type of atomic force microscope (AFM) cantilever employed for a specific experimental application is often crucial to the success or failure of the intended measurement. The range of AFM cantilevers currently commercially available is greater than ever and offers the experimentalist a phenomenal choice of probe with which to work. AFM cantilevers are typically fabricated from silicon and silicon nitride, with various tip shapes, aspect ratios, and tip modifications available, allowing imaging with excellent resolution. Cantilevers can be purchased with reflective gold and aluminium coatings, magnetic cobalt alloy coatings, electrically conductive platinum–iridium coatings, whilst cantilever tips are often found coated with gold in preparation for chemical modification and coated with a diamond-like thin film for applications where tips require high wear resistance. However, whilst there exist AFM cantilevers with spring constants on the order 0.01 N/m for applications requiring picoNewton force sensitivity, there are remarkably few cantilevers with spring constants larger than 20–50 N/m. With AFM manufacturers offering piezoelectrically actuated fixed-end displacements of 100 μm and greater, there now exists a force regime on the order 1–10 μN, which represents an upper limit given currently commercially available cantilevers. This limitation applies in both tension and compression, and therefore if cantilevers with spring constants on the 100–1000 N/m could be fabricated, this would afford the vertical displacement sensitivity of AFM to integrate with the possibility of measuring forces up to the milliNewton regime.

Whilst AFM cantilevers have been traditionally made from silicon or silicon nitride due to the ease at which they are fabricated using standard MEMS techniques, polymers, such as SU-8 have been shown to be a promising alternative [1,2]. Polymers have always been useful in various MEMS fabrication processes, usually as a mask or sacrificial layer [3], but with the recent development of polymers with excellent mechanical properties and chemical stability they are increasingly being used as a structural material [4]. Polymeric materials typically have a Young's modulus and density lower than their silicon-based counterparts [5]. This results in cantilevers with high mass [1] and surface stress [6] sensitivity. These mechanical attributes, coupled with polymers ability to absorb chemicals and accept surface modifications such as gold–thiol chemistry and direct coating with analyte molecules [6] has lead to polymeric cantilevers being used for a number of chemical sensing [7] and biosensing applications [8].

As polymers can be developed to have a wide range of properties, cantilevers can be fabricated to suit almost any purpose using a range of methods [9–11] allowing for wafer scale production [12]. Photosensitive polymers have allowed for the integration of electronics directly into the polymer [5,13] and the embedding of ferromagnetic and paramagnetic nanoparticles to

* Corresponding author.
E-mail address: D.Cheneler@bham.ac.uk (D. Cheneler).

0304-3991/$ - see front matter © 2011 Elsevier B.V. All rights reserved.
doi:10.1016/j.ultramic.2011.03.009

form composites [14]. This has lead to a departure from the traditional AFM actuation and sensing method of using piezoelectric stages and optical systems [15]. Electrostatic, thermal, strain gauge and magnetic methods are being used in increasing numbers of applications [13–15]. This has meant AFM is not limited to monitoring the response of a single cantilever in a transparent medium but can measure the response of a high density array of cantilevers in an opaque medium such as blood [13].

However, current polymer cantilevers still have a number of limitations. Common polymers such as SU-8 have a Young's modulus up to 30 times less than silicon [5]. While this makes them more sensitive it means the range of forces that can be measured with these cantilevers is low. Their material properties also mean that the Q-factor of these cantilevers is very low (<20 [16]). Even with Q-enhancement, such as positive feedback methods, the Q-factor is usually *c.a.* 100 [1]. This is because polymeric cantilevers are inherently viscoelastic resulting in high internal viscous losses [4] and creep [17]. There are also a number of fabrication issues with polymers including high residual stresses, surface cracks and air inclusions [9,11].

To this end, a new, commercially viable, fabrication method for polymer cantilevers using Direct Digital Manufacturing (DDM) technology is proposed. DDM technology is manufacturing process, which allows for the creation of physical components directly from 3D Computer Aided Design (CAD) data using computer-controlled additive fabrication techniques. DDM technology has been used previously to manufacture components for an AFM but never for the AFM cantilevers themselves [18]. The cantilevers detailed here are fabricated from a resin which forms a linear, highly elastic glassy polymer with superior mechanical properties to conventionally used polymers. The method used results in cantilevers with a cylindrical cross-section leading to increased stiffness and force range. As they can be fabricated with lengths longer than most polymer AFM cantilevers, they can be shown to have greater deflection sensitivity. They can also support larger probes without suffering excessive deflection [19] allowing for more sensitive and accurate measurements during indentation experiments.

In this paper the fabrication of these cantilevers are described. Due to the issues that other polymer cantilevers have with transient material properties, the resin was tested to show that it is a highly linear elastic material exhibiting negligible creep. As these cantilevers have a circular cross-section, their stiffnesses and natural frequencies have been calculated using Timoshenko beam theory which extends the more usual Euler–Bernoulli beam theory by taking into account shear and rotary inertia effects. As the exact solutions are rather involved, more convenient approximate solutions have been given and derived in Appendix A. The expressions detailing the effect of metallisation and varying radius on the cantilevers performance have also been derived. Prototype cantilevers were then installed in an AFM and their dynamic response measured and compared to theoretical predictions.

2. Cantilever fabrication

The DDM technique chosen for cantilever fabrication was Micro-stereolithography (MSL). The technique of MSL is capable of producing precision micro-components with dimensions in the sub-millimetre regime [20]. A CAD drawing (see Fig. 1) of the required component is sliced horizontally to create a set of digital images, that when layered together, represent the final component. The MSL apparatus then utilises either a direct write laser source or dynamic mask projection system to solidify a

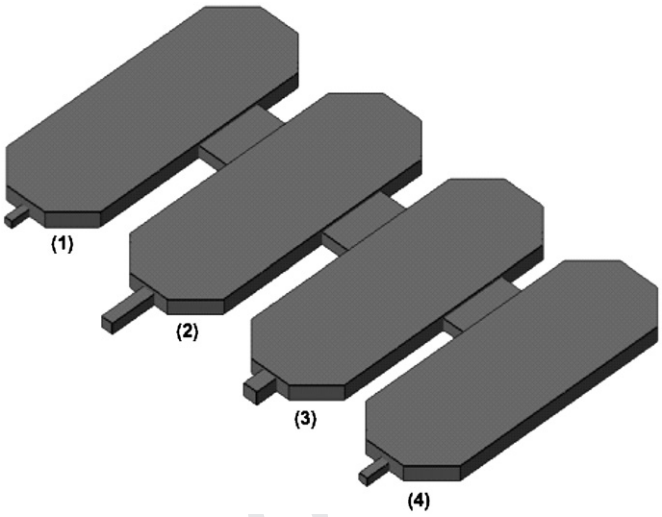

Fig. 1. CAD designs of cantilevers rendered using Meshlab.

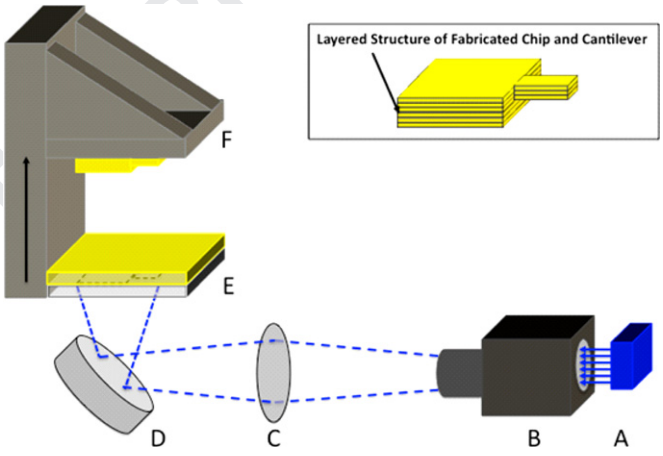

Scheme 1. Scheme depicting the MSL system used. (For interpretation of the references to color in this figure legend, the reader is referred to the web version of this article.)

photosensitive polymer resin, in an additive, layer-by-layer fashion based upon these digital images. The final component is composed of a number of layers of resin of uniform thickness. The power of the technique for fabricating micro-components such as AFM cantilevers is in the precise control over the thickness of each individual resin layer that can be achieved. Furthermore, components such as AFM cantilevers can be fabricated to the requirements of the experimentalist in a matter of minutes, without the requirement for any complicated tooling or etching.

The system used here was custom-built projection MSL system, based around a Digital Micromirror Device (DMD) digital projector. Briefly, the system comprises a blue LED light engine (ENFIS, UK, Uno AIR LE, Spectral output maxima at 465 nm) (Scheme 1A), a DMD projector (Compaq MP1800) (Scheme 1B), focussing optics (Scheme 1C), 45° mirror (Scheme 1D), custom made silicone resin tray (Scheme 1E) and a glass platform mounted on three linear motion stages (**X**, **Y** and **Z**) (Aerotech UK, (**X** and **Y**) ALS130-100 (**Z**) ALS130-050) (Scheme 1F). The custom control software for the MSL system was written in C♯.

After each layer of resin was cured by the projection source, the glass platform is moved upwards 15 μm and another layer of resin cured to the previous one. The photosensitive polymer resin

used for fabrication of the cantilevers was a custom formulation. The resin was composed of poly(ethylene glycol) diacrylate (PEG, Sigma Aldrich, UK, Average MW:575) as a monomer, dipentaerythritol penta-/hexa-acrylate (DPHA, Sigma Aldrich, UK) as a cross-linker and Irgacure 784 (PI, BASF), a titanocene based radical photoinitiator. The components of the resin were used in the ratio of 40:10:1 (PEG:DPHA:PI) by weight%. After fabrication, the cantilevers were coated on one side with a layer of silver in an Auto 306 evaporator (Edwards, UK) to improve the reflectivity of the resin. The thickness of the silver coating (100 nm) was measured using a quartz crystal microbalance housed within the evaporator chamber.

Table 1 shows the designed dimensions of the cantilevers and the actual dimensions of the fabricated cantilevers. The differences between the designed dimensions and the observed dimensions is due to (a) the interpretation of the CAD data by the software used to create the mask images sent to the digital projector (e.g. determining whether a feature falls within the current pixel or the neighbouring pixel) and (b) dimensional changes in the resin upon curing. The cantilevers were designed with a square cross-section, however, blurring (the presence of grey pixels instead of black or white pixels) at the edges of the features in the mask images and surface tension effects leads to rounded edges on components. Due to the small size of fabricated cantilevers, these rounded edge phenomenon leads to the cantilever having an apparent circular cross-section. The dimensional differences and effects on cross-section shape can be improved upon by pre-processing of mask images to improve pixel recognition and remove grey pixels at the edge of features. Cantilevers fabricated using these improvements and having a more regular cross-section shape will be presented in a future paper. Fig. 2 shows an optical microscopy image of a typical circular cross-section cantilever fabricated and an optical microscopy image of a section cantilever showing its circular cross-section. There is a slight amount of damage to the upper left section of the cantilever due to the sectioning of the cantilever using a scalpel blade.

Table 1
The designed and actual geometry of the manufactured prototype cantilevers. The aspect ratio is defined as the ratio of the cantilever radius to its length.

Cantilever	Designed width (μm)	Designed length (μm)	Actual diameter (μm)	Actual length (μm)	Aspect ratio
1	115	300	90	278	0.32
2	180	720	156	705	0.22
3	220	340	196	318	0.62
4	130	380	102	360	0.28

3. Theory

As the beam can be fabricated to have a wide range of length to radius ratios, a situation may occur whereby the assumptions used in standard beam theory are invalid [21]. This will typically happen when the beam is 'stocky', i.e. the ratio between the beam's radius and length is high. In these cases shear stresses, which are usually neglected in standard Euler–Bernoulli beam theory become important and need to be taken into account. Therefore Timoshenko beam theory is more appropriate for these beams [21]. Timoshenko beam theory extends the usual Euler–Bernoulli beam equations (which assumes the beam is in pure bending) to include shear deformation and rotational inertia effects. Typically taking into account the other mechanisms lowers the stiffness of the beam its resonant frequency [22].

As shown in Appendix A the stiffness of the cantilever based on Timoshenko beam theory can be shown to be

$$K = \left(\frac{L^3}{3EI} + \frac{L}{AkG}\right)^{-1} \tag{1}$$

or

$$K = \frac{3\pi EkR^4}{2L(2L^2k + 3(1+\upsilon)R^2)} \tag{2}$$

where A is the cross-section area, L is the beam length, R is its radius, E is Young's modulus, G is the shear modulus, υ is Poisson's ratio of the beam, I is the second moment of area and k is the Timoshenko shear coefficient.

Whilst there are exact solutions for the governing differential equations for the dynamics of Timoshenko beams [22], they are complicated and inconvenient for experimental characterisation of AFM cantilevers. Therefore an approximate solution has been derived in Appendix A, which shows how Rayleigh's method for calculating the resonant frequency of beams [23] has been modified to include shear stress and rotary inertia effects and so gives the approximate resonant frequency for Timoshenko beams. The resonant frequency, in Hz, can thus be shown to be

$$f = \frac{1}{2\pi}\sqrt{\frac{140EIGk(AkGL^2 + 3EI)}{\rho L^2(11L^4(AkG)^2 9 + 77L^2EIAkG + 140(EI)^2 + 56L^2IA(kG)^2)}} \tag{3}$$

where ρ is the density of the material. Eqs. (1)–(3) are valid for cantilevers of any cross-section as long as that cross-section is constant along its length. For the specific case of cylindrical cantilevers, the cross sectional area given is by

$$A = \pi R^2 \tag{4}$$

and the second moment of area given by

$$I = \frac{\pi}{4}R^4 \tag{5}$$

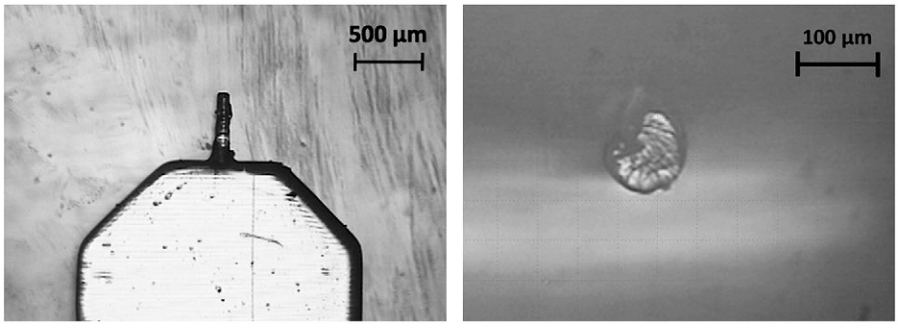

Fig. 2. Optical microscopy image of a typical fabricated cantilever and sectioned cantilever showing a circular cross-section.

Please cite this article as: D. Cheneler, et al., Ultramicroscopy (2011), doi:10.1016/j.ultramic.2011.03.009

The shear coefficient is shape-dependent. For a circular cross-section it is given as [24]

$$k = \frac{6(1+\upsilon)^2}{7+12\upsilon+4\upsilon^2} \tag{6}$$

It can be seen in Eqs. (1) and (3) that the stiffness and resonant frequency of a cantilever is strongly dependent on the flexural rigidity of the cantilever given by EI. As AFM cantilevers frequently need to be coated, either to functionalise them or make them more reflective as is the case here, the effect of the coating on the flexural rigidity may need to be taken into account. In Appendix B, the situation where the resin cylindrical cantilever is coated on the top surface with a silver layer is considered. While this analysis is valid for all layer thicknesses, typically the silver layer is thin and it can be shown that for most practical situations the effect of the silver coating can be neglected. For example, a 100 nm thickness layer of silver on a cantilever of length 500 μm and radius 50 μm would change $K=27.38$ by 0.01 N/m and $f=24.54$ kHz by 10 Hz. The coating only really needs to be considered when the thickness of the layer is comparable to the radius of the cantilever.

As this method of fabrication can be used to make cantilevers of any cross-section, it is interesting to note the situation where the radius of the beam varies linearly along its length, i.e. the beam is conical. In this case, due to the additional complications of the varying cross-section, it is necessary to neglect shear and rotary inertia effects in order to keep the analysis simple. This assumption becomes accurate when the cantilever's radius to length ratio is small. The mechanics of a conical cantilever are derived in Appendix C. The stiffness of a conical cantilever with fixed end radius R_1 and free end radius R_2 can be shown to be

$$K = \frac{3\pi E}{4L^3} R_2 {R_1}^3 \tag{7}$$

It can also be shown that the resonant frequency, in Hz, of a conical cantilever is

$$f = \left[\frac{30E}{4\pi^2 L^4 \rho}\frac{R_1^3(R_1-R_2)^7}{R_2}\left((R_1-R_2)[18R_1^6+39R_1^5R_2+57R_1^4R_2^2-123R_1^3R_2^3 + 107R_1^2R_2^4-46R_1R_2^5+8R_2^6]+60R_1^6R_2\ln\left(\frac{R_2}{R_1}\right)\right)^{-1}\right]^{1/2} \tag{8}$$

Furthermore it can be shown that in the limit where $R_2 \to R_1$ so that $R_1=R_2=R$

$$f = \left(\frac{385ER^2}{484\pi^2 L^4 \rho}\right)^{1/2} \tag{9}$$

This last expression will equal Eq. (3) when shear and rotary effects become negligible i.e. when the cantilever's radius to length ratio is sufficiently small.

4. Experimentation

Cantilever dimensions were measured using a WiTec Alpha 300R Confocal Raman Microscope (LOT Oriel, UK) through a 20X lens. The frequency response of the cantilevers was obtained through base excitation of a cantilever specimen whilst secured in a NanoWizard II AFM (JPK Instruments, UK). The uncertainty was ±10 Hz for the frequency measurements and ±0.3 mV for the amplitude.

The stiffness of the cylindrical cantilevers was measured by deflecting them vertically downwards using a rectangular Si AFM cantilever of spring constant 19.6 ± 1.3 N/m (MikroMasch, Estonia), calibrated according to [19], by moving the fixed end of the Si cantilever at a velocity of 0.2 μm/s. Care was taken to minimise the lateral deflection of the Si cantilever during the measurement in order that the maximum force was distributed normally between cantilevers. The force required was measured directly from the vertical deflection of the Si cantilever, whilst the deflection of the cylindrical cantilever was calculated from the difference between the motion of the fixed end of the Si cantilever and the measured vertical deflection. The fixed end had a 15 μm travel range driven by a 440 V supply from an ultra precise 24 bit ADC. The photo detector has a 16 bit ADC with a 20 V range and a calibrated voltage sensitivity of 26.117 nm/V. The resultant uncertainty in the measured deflection in this case is therefore ±8 pm.

For instance, in Fig. 3 the AFM data from the testing of cantilever 2 is given. As the dashed red lines indicate, the deflection of the Si cantilever was 15 nm for a fixed end motion of 20 nm, resulting in a deflection of the resin cantilever of 5 nm. Given that the stiffness of the Si cantilever was 19.6 ± 1.3 N/m, the force applied to the resin cantilever was 294 ± 19.5 nN therefore the stiffness of cantilever 2 must be 294 nN/5 nm = 58.8 ± 3.9 N/m.

The true density of the photocured resin was measured using an AccuPyc II 1340 Helium Pycnometer (Micromeritics, UK) and is given as 1.220 ± 0.002 g/cm^3. The reduced modulus of the resin was measured using a NanoTest nanoindenter (Micro Materials, UK) employing a diamond-coated Berkovich indenter and calculated to be 309 ± 9 MPa. The indentation was performed perpendicular to the direction of the layers within the resin structure and repeated 25 times, each in a different unperturbed area, and

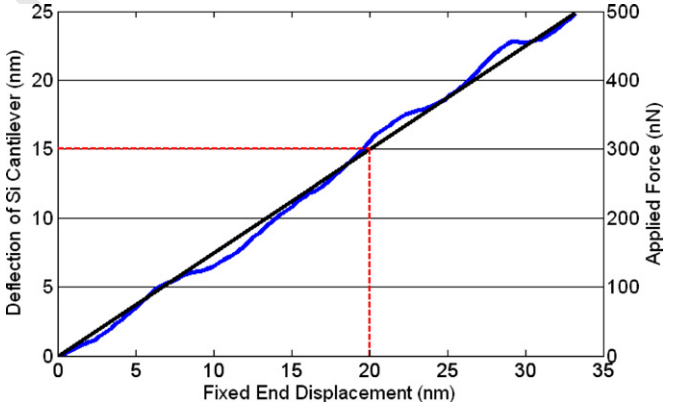

Fig. 3. AFM deflection curve for cantilever 2. The black straight line gives the fitted gradient. Note the waviness of the curve is due to optical interference from the Si cantilever.

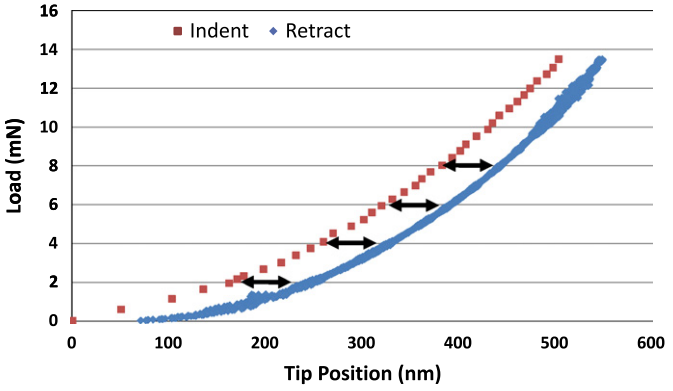

Fig. 4. Typical indentation data for the resin. The black arrows denote the equal distance between the indent and retract curves emphasising that no creep or hysteresis was observed.

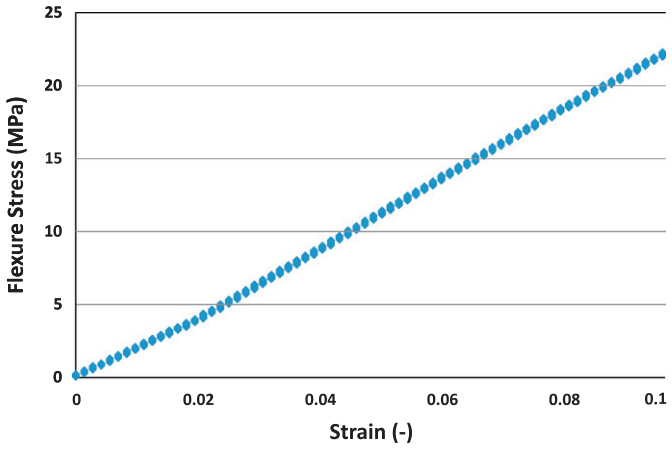

Fig. 5. Typical four-point bending test data showing the linear behaviour of the material up to strains of 10%.

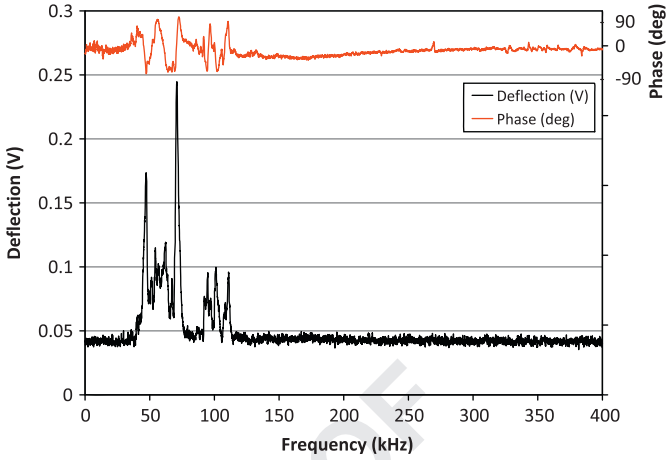

Fig. 6. Typical experimental frequency response spectrum for a cylindrical cantilever.

averaged. In Fig. 4, the data from a typical indentation is given. The indentation hold time was 30 s and as can be seen in Fig. 4, the elastic recovery is exactly the total penetration depth minus the initial plastic deformation. This shows that no creep or hysteresis was observed during the indentation test, as denoted by the indent and retract curves being parallel. The elastic modulus of the resin was measured by four-point bend testing of rectangular resin specimens using a MicroTest 5848 mechanical tester (Instron, UK). The value for which was calculated to be 244 ± 5 MPa and with the reduced modulus, gives a Poisson's ratio of 0.48 ± 0.002. The stress/strain data given in Fig. 5 from the four-point bending test shows that the material is linear at least up to strains of 10%.

5. Results and discussion

In order to ascertain the frequency response of the cantilevers, and hence their resonant frequencies, the cantilevers were excited by using the base-excitation method whilst the tip deflection was monitored. A typical spectrum showing the phase and amplitude of the deflection as a function of frequency, in this case for cantilever 1, is shown in Fig. 6.

The spectra resulting from the frequency sweep performed on the cylindrical cantilevers were noisy and showed small peaks in places which could not be ascribed to any particular bending mode. Such artefacts are common in frequency sweep spectra for silicon AFM cantilevers, but are of much smaller amplitude than the actual resonance peaks observed for the cantilever of interest. The cylindrical cantilevers are of greater mass than standard silicon and silicon nitride AFM cantilevers, and therefore required a greater amplitude of fixed end excitation in order to achieve resonance peaks above the noise level of the system. Hence, these spectra appear slightly noisy in comparison to those typically obtained for standard AFM cantilevers. The resonant frequency was taken to be the frequency with the highest peak. It is to be noted that while the silver coating on the resin cantilevers was highly reflective and improved the sum signal intensity, it was still found to be lower than that typically achieved for a silicon cantilever or gold-coated silicon nitride cantilever owing to the curvature of the beam. Whilst lower, as the diameter of the cantilevers was large, the intensity was still sufficient for experimentation.

Some of the extra peaks may not necessarily be due to noise but may be due to the effect of other mode shapes. To see how having cylindrical geometry affects the mode shapes of the cantilevers, eigenvalue analysis was performed using the finite element method with the MEMS module in Comsol Multiphysics version 3.5 (Comsol Inc. USA). In Fig. 7 the first six mode shapes are shown along with the pertinent resonant frequencies. It is clearly seen that, due to the symmetry of the cantilevers, when the mode shape is not axisymmetric there are multiple similar mode shapes at the same frequency. For instance, modes 1 and 2 in Fig. 7 are both bending modes with one deflecting in plane and the other out of plane with both mode shapes occurring at the same frequency, the discrepancy here being likely due to numerical error. Any asymmetry in the fabrication of the cantilevers will cause the actual frequencies at which these modes to occur to separate. This could explain the two strong peaks seen the spectra in Fig. 6. The out of plane bending mode will always give a lower amplitude but finite signal in the AFM because even though it is not deflecting vertically, the laser will move vertically as the cantilever moves side to side due to the curvature of the cantilever. For similar reasons there may be some peaks due to the other mode shapes, even though the cantilever is not bending vertically, but their amplitude will be very small.

Numerical values for the resonant frequency were also obtained using finite element methods to perform eigenvalue analysis. The resonant frequencies obtained were compared to those calculated analytically from Eq. (9), which is the frequency calculated from Euler–Bernoulli beam theory, and Eq. (3), which is calculated from an approximation of Timoshenko beam theory. These values, along with those obtained from experiment, are given in Table 2.

The values given in Table 2 show that the approximation of Timoshenko beam theory, given by Eq. (3), gives a result very close to that obtained numerically. It is certainly a more accurate formulation than that calculated using standard Euler–Bernoulli theory. Interestingly Eq. (3) always slightly underestimates the numerical value. This is likely to be because it was assumed that the static deflection of the cantilever as calculated from Timoshenko beam theory was the same as the dynamic deflection of the cantilever at the resonant frequency, whereas there are likely to be small deviations between the two. Despite this, the agreement between values calculated using Eq. (3) and the experimentally measured values are within 10% and hence Eq. (3) is a good approximation.

During experimentation, the Q-factor of a cantilever is often an important parameter as it describes how sharp a resonant peak will be and so how accurate the resonant frequency can be measured. As data is often represented in spectra as exemplified in Fig. 6, the Q-factor is most easily defined as the resonant

Please cite this article as: D. Cheneler, et al., Ultramicroscopy (2011), doi:10.1016/j.ultramic.2011.03.009

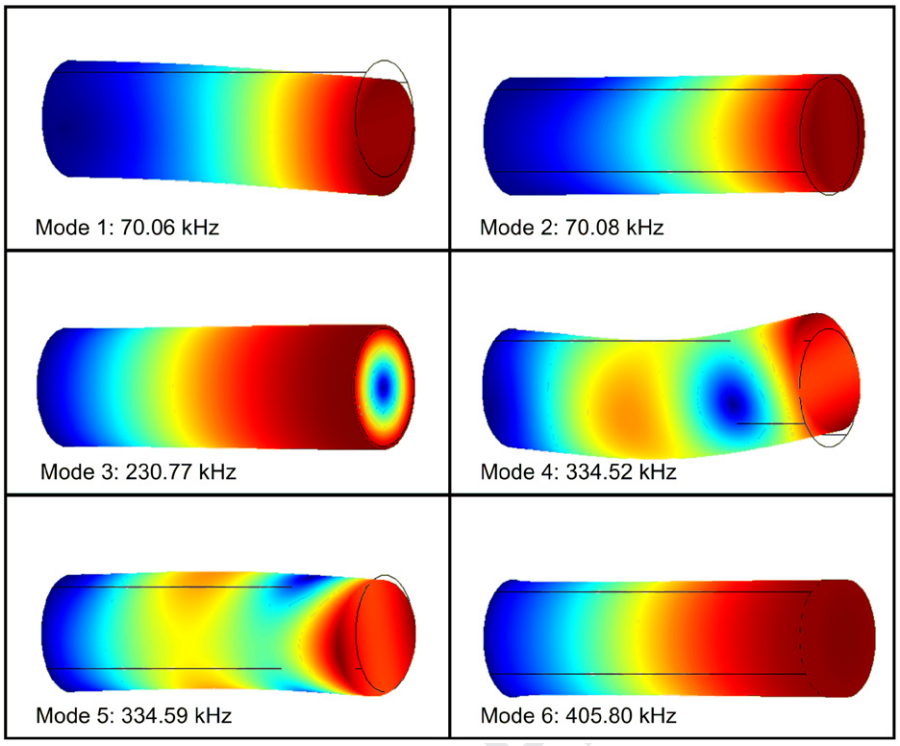

Fig. 7. The first six numerically calculated mode shapes for a cylindrical cantilever. The frequencies at which they occur are given for cantilever 1.

Table 2
Resonant frequencies as obtained from theory, numerical analysis and experiment. *E.–B.* stands for Euler–Bernoulli beam theory and Timo. is an abbreviation for Timoshenko beam theory. The error describes the discrepancy between the approximate Timoshenko beam theory and experiment. Experimental uncertainty is ± 10 Hz.

Cantilever	Resonant frequency (Hz)				Error (%)
	Theoretical		Numerical	Experimental	
	E.–B. Eq. (9)	Timo. Eq. (3)			
1	73.27	69.45	70.06	70.70	−1.77
2	19.67	19.17	19.30	18.00	6.50
3	120.86	102.47	104.49	96.60	6.08
4	49.34	47.33	47.82	46.30	2.22

Table 3
Cantilever stiffnesses as obtained from theory, numerical analysis and experiment. *E.–B.* stands for Euler–Bernoulli beam theory and Timo. is an abbreviation for Timoshenko beam theory. The error describes the discrepancy between the Timoshenko beam theory and experiment. Q7

Cantilever	Stiffness (N/m)				Error (%)
	Theoretical		Numerical	Experimental	
	E.–B. Eq. (7)	Timo. Eq. (1)			
1	107.42	101.42	103.11	98.00 ± 6.45	3.49
2	59.19	57.58	58.91	58.80 ± 3.88	−2.07
3	1575.04	1293.86	1309.36	744.80 ± 49.17	73.72
4	71.29	67.69	69.48	65.30 ± 4.31	3.66

frequency divided by the bandwidth, or range of frequencies with values above half the value at the resonant frequency. The Q-factors for cantilevers from 1 to 4 can therefore be given as 13.9, 10.8, 13.05 and 13.6, respectively. These values are low compared to commercial silicon AFM cantilevers, but comparable to other polymeric AFM cantilevers which have Q-factors generally less than 20 [16]. As most existing polymeric cantilevers are made from SU-8 or similar, the low Q-factor of those cantilevers is likely due to internal damping due to the materials viscoelastic nature. Whilst the cantilevers described in this paper are likely to suffer from some manner of internal loss, it is less likely to be due to internal viscous losses as the resin these cantilevers are made of is highly elastic as discussed in Section 4. However, due to the increased size and inertia of these cantilevers, the effects of air damping and loss to the cantilever anchor are likely to be more pronounced.

Due to the low Q-factor of these cantilevers, they are better suited to AFM-based depth sensing indentation experiments where the force being applied to the cantilevers may be large. It is therefore necessary to know the stiffness of the cantilevers quite accurately. To this end the analytical values for the stiffness, calculated using Euler–Bernoulli beam theory, given by Eq. (7), and Timoshenko beam theory, given by Eq. (1), are compared to numerically and experimentally measured values. For this purpose numerical analysis was performed using the static solver in the same module as before. The values are given in Table 3.

Again the Timoshenko beam theory, given by Eq. (1), closely approximates the values given by the numerical analysis. In general there is also good agreement between the values measured experimentally, using the method described in Section 4, and the theory. However, the measured stiffness for cantilever 3 is significantly lower than the calculated stiffness, a result which can be explained from the large relative difference between the spring constants of the two cantilevers. The maximum possible vertical deflection which could be applied to the cylindrical cantilever was limited by the maximum measurable vertical deflection of the silicon cantilever, which is restricted to the maximum vertical range of the AFM photodiode. Therefore, for a large vertical deflection of the silicon cantilever, only a small vertical deflection could be applied to the cylindrical cantilever.

Please cite this article as: D. Cheneler, et al., Ultramicroscopy (2011), doi:10.1016/j.ultramic.2011.03.009

Another possible issue is the potential indentation of the silicon cantilever into the resin cantilever during calibration, as this may affect the accuracy of the accuracy the stiffness measurement. The geometry of the cantilever/cantilever contact during stiffness testing was with the tipless silicon cantilever lowered onto the cylindrical resin cantilever. The cantilevers were held perpendicular to each other, ensuring that the entire width (35 μm) of the silicon cantilever was above the resin cantilever. Assuming Young's modulus and Poisson's ratio of the silicon cantilever was 160 GPa and 0.27, respectively [26] and the expression for the indentation of a cylinder by a flat plane as given in [27], the indentation depth of cantilever 2 after the 500 nN contact was calculated to be 57.5 pm. This is representative of all the stiffness measurements and shows that the error in these tests is still dominated by the error in the silicon cantilever calibration and that the effect of indentation is negligible.

As these cantilevers are intended for use in indentation experiments, it is necessary to attach a tip to the end of the cantilevers. Generally there are two types of tip used for indentation, namely sharp pyramidal tips [28] and spherical probes [29]. Whilst it will not be possible to fabricate tips which are hard and sharp compared to single crystal materials using DDM, the fabrication of spherical probes is quite a simple task, given the layout of the cantilevers as shown in Fig. 1. These spheres will be realised in exactly the same way as the cantilevers with the shape being built up in layers as described. However, as single crystal probes and tips will generally have better material and geometric properties than can be realised using polymeric materials, it may be preferable to attach these probes to the cantilevers after fabrication. Fortunately this is common practice for both diamond tips [30,31] and spherical probes [32,33]. In all these cases the tip if fabricated separately in various ways depending on material and geometry and glued to the cantilever.

There are some factors that should be considered when applying Eqs. (1) and (7) to cantilevers made using this fabrication method. For instance, in order to make the top surface of the cantilevers reflective, a thin layer of silver was sputtered onto it. Whilst every attempt was used to minimise any effects of this, metal sputtering is a high energy process which can affect the polymer and may even induce additional stress into the cantilever, causing it to curve, affecting results. Alternative methods, for example chemical vapour deposition or implanted reflective nanoparticles, may be more suitable and reduce the chances of inducing stress. It is also to be noted from the image of the cantilevers shown in Fig. 2 that the material is layered resulting in a slight anisotropy in the material properties. The effect of this is negated by measuring the effective modulus of the layered medium, as discussed in Section 4, rather than a block of the unprocessed resin. Fig. 2 also shows a slight increase in radius of the cantilever near the base. As the stiffness is highly dependent on the radius, care needs to be taken to ensure this increase is minimised or at least that the length used in the theory is chosen appropriately as otherwise the predicted stiffness will be lower than actuality.

The advantages of MSL for the fabrication of AFM cantilevers is in the ability to rapidly produce cantilevers of the required dimensions without any pre-tooling or lengthy fabrication stages. As with all DDM processes, MSL is a technology that can bring fabrication closer to the end user of the component being manufactured, giving them more power and freedom in the design and fabrication of components. For example, an MSL machine could sit in a laboratory next to an AFM and be used to fabricate a new set of cantilevers every time they were required and with the exact dimensions and characteristics required for the current experiment.

The limitations of MSL arise from the minimum feature size achievable with the system used and the range of materials that can be used. The minimum addressable voxel (volumetric pixel) size is due to the resolution of the digital projector used, the focussing optics and the step size of the linear motion stage. The materials used are limited to a polymer resin system that can be cured using a photoinitiator, however the resin can be doped with chemical species or nanoparticulates to achieve a wide and varied range of materials and material properties. Cantilevers and components can be fabricated in almost any shape, orientation or package as the process is not confined by conventional manufacturing considerations. Components that are difficult or even impossible to fabricate through more traditional techniques are easily achievable with MSL.

6. Conclusion

Atomic force microscope cantilevers have been fabricated using Direct Digital Manufacturing techniques and tested. They have been analysed theoretically using an approximation of Timoshenko beam theory and results for the stiffness and resonant frequency of the cantilevers show good correlation with experimentally measured values. It has been shown that cantilevers fabricated in this manner can have stiffnesses much higher than commercially available silicon cantilevers, allowing for experimentation in a force regime orders of magnitude higher than currently possible using the AFM making them uniquely appropriate for indentation experiments.

Acknowledgements

The Atomic Force Microscope, Confocal Raman Microscope, Nanoindenter, Mechanical Tester, Helium Pycnometer and Micromanipulator used in this research were obtained, through Birmingham Science City: Innovative Uses for Advanced Materials in the Modern World (West Midlands Centre for Advanced Materials Project 2), with support from Advantage West Midlands (AWM) and part funded by the European Regional Development Fund (ERDF). The authors would also like to thank Dr. J.A. Covington assistance with laboratory space and equipment and for useful discussion.

The contributions were: DC derived the analytical model for the mechanical behaviour of the cylindrical cantilevers, and performed finite element modelling. JB performed the AFM analyses, nanoindentation, density measurement and four-point bend testing. SJL designed and manufactured the cylindrical cantilevers. SJL, CPP, DRB and DAH funded, designed and manufactured the MSL equipment. MCLW provided financial support for DC.

Appendix A. Timoshenko beam theory

The full Timoshenko beam equations can be expressed as two coupled linear partial differential equations [21]:

$$\rho A\frac{\partial^2 u}{\partial t^2}=\frac{\partial}{\partial x}\left(AkG\left(\frac{\partial u}{\partial x}-\theta\right)\right) \tag{A1}$$

$$\rho I\frac{\partial^2 u}{\partial t^2}=\frac{\partial}{\partial x}\left(EI\frac{\partial \theta}{\partial x}\right)+AkG\left(\frac{\partial u}{\partial x}-\theta\right) \tag{A2}$$

where ρ is the density of the material, A is the cross-section area given by $A=\pi R^2$, u is the deflection, θ is the angular displacement, E is Young's modulus, G is the shear modulus, I is the second moment of area given by $I=(\pi/4)R^4$ and k is the Timoshenko shear coefficient.

The shear coefficient is shape-dependent. For a circular cross-section it is given as [24]

$$k=\frac{6(1+\upsilon)^2}{7+12\upsilon+4\upsilon^2} \tag{A3}$$

where υ is Poisson's ratio of the beam.

For a static beam, Eqs. (1) and (2) can be simplified to

$$0=\frac{\partial}{\partial x}\left(AkG\left(\frac{\partial u}{\partial x}-\theta\right)\right) \tag{A4}$$

$$0=\frac{\partial}{\partial x}\left(EI\frac{\partial \theta}{\partial x}\right)+AkG\left(\frac{\partial u}{\partial x}-\theta\right) \tag{A5}$$

These equations can be uncoupled by differentiating Eq. (5) with respect to x and rearranging it to gives

$$\frac{\partial}{\partial x}\left(AkG\left(\frac{\partial u}{\partial x}-\theta\right)\right)=-\frac{\partial^2}{\partial x^2}\left(EI\frac{\partial \theta}{\partial x}\right) \tag{A6}$$

Substituting this into Eq. (4) gives

$$\frac{\partial^2}{\partial x^2}\left(EI\frac{\partial \theta}{\partial x}\right)=0 \tag{A7}$$

This should be recognised as the Euler–Bernoulli beam equation and takes into account the bending stresses. Rearranging Eq. (5) gives the second equation to be solved

$$\frac{\partial u}{\partial x}=\theta-\frac{1}{AkG}\left(\frac{\partial}{\partial x}\left(EI\frac{\partial \theta}{\partial x}\right)\right) \tag{A8}$$

This also reduces to the Euler–Bernoulli beam theory when the second term on the right equals zero. Physically it can be seen that shear effects cause the angle of the cross-sectional planes to change from being perpendicular from the neutral axis (a basic assumption in the formulation in the Euler–Bernoulli beam theory). The static deflection of a cantilever with uniform cross-section as predicted by Timoshenko beam theory can be shown to be [25]

$$u(x)=\frac{Px}{6EI}(3Lx-x^2)+\frac{Px}{AkG} \tag{A9}$$

where L is the length of the beam and P is the concentrated load applied at the free end of the cantilever.

Given Eq. (9) the stiffness can be shown to be

$$K=\left(\frac{L^3}{3EI}+\frac{L}{AkG}\right)^{-1} \tag{A10}$$

or

$$K=\frac{3\pi EkR^4}{2L(2L^2k+3(1+\upsilon)R^2)} \tag{A11}$$

The natural frequency of a beam can be approximated using Rayleigh's method [23]. This method assumes the first mode shape is equal to the static deflection of the cantilever and uses this deflection to calculate the kinetic and potential energy in the beam during resonance. The total kinetic energy of a stocky beam including rotary inertia can be shown to be

$$T=\frac{1}{2}\int_0^L \rho A\left(\frac{\partial U(x,t)}{\partial t}\right)^2+\rho I\left(\frac{\partial \Theta(x,t)}{\partial t}\right)^2 dx \tag{A12}$$

where $U(x,t)=u\cos\omega t$, $\Theta(x,t)=\theta(x)\cos\omega t$ and ω is the angular frequency in rad/s. The angular displacement can be given by the integration of Eq. (7) to give

$$\theta(x)=\frac{Px}{2EI}(x-2L) \tag{A13}$$

In a similar fashion, the potential energy of the cantilever including shear deformation can be shown to be

$$U=\frac{1}{2}\int_0^L EI\left(\frac{\partial \Theta(x,t)}{\partial x}\right)^2+AkG\left(\Theta(x,t)-\frac{\partial U(x,t)}{\partial x}\right)^2 dx \tag{A14}$$

Equating the maximum values of Eqs. A12 and A13, found when $\sin\omega t=1$, and solving for angular frequency gives

$$\omega^2=\frac{\int_0^L EI(\partial\theta(x)/\partial x)^2+AkG(\theta(x)-(\partial u(x)/\partial x))^2 dx}{\int_0^L \rho Au(x)^2+\rho I\theta(x)^2 dx} \tag{A15}$$

Substituting in Eqs. A9 and A13 and solving gives the approximate resonant frequency of a stocky beam as

$$f=\frac{1}{2\pi}\sqrt{\frac{140EIGk(AkGL^2+3EI)}{\rho L^2(11L^4(AkG)^2 9+77L^2EIAkG+140(EI)^2+56L^2IA(kG)^2)}} \tag{A16}$$

Eqs. A10 and A16 are valid for beams with any constant cross-section and be shown to reduce down to the solutions given by the standard Euler–Bernoulli beam theory when the cantilever thickness to length ratio is small.

Appendix B. The effect of the coating on the flexural rigidity of the cantilever

The flexural rigidity of a coated cylindrical cantilever can be calculated using the composite beam method. This method states that at the neutral axis (see Fig. B1), all forces due to bending stresses are in equilibrium, i.e.

$$\sum F=0=\int_A \sigma_b dA=\int_{A,Re}\sigma_{b,Re}dA_{Re}+\int_{A,Ag}\sigma_{b,Ag}dA_{Ag} \tag{B1}$$

where A is the cross-sectional area of each layer and σ_b is the bending stress given by $(-EY/\rho)$, where ρ is the radius of curvature, y is the distance to the neutral axis and E is Young's modulus of the layer. *Re* and *Ag* denote the resin and silver components, respectively.

Substituting the expression for the bending stresses into the force balance above gives

$$\begin{aligned}0&=\int_{A,Re}\frac{E_{Re}y_{Re}}{\rho}dA_{Re}+\int_{A,Ag}\frac{E_{Ag}y_{Ag}}{\rho}dA_{Ag}\\&=E_{Re}y_{Re}A_{Re}+E_{Ag}y_{Ag}A_{Ag}\\&=E_{Re}(R-y_c)\pi R^2+E_{Ag}(R+\bar{y}_{Ag}-y_c)\frac{\pi}{2}(R'^2-R^2)\end{aligned} \tag{B2}$$

where $R'=R+t$ and $\bar{y}_{Ag}$ is the distance between the centroid of the silver layer and the centre of the arc as shown in Fig. B2

This can be found in the usual way by using the integral method to find the centroid of the two semicircles and then using geometric decomposition to find the centroid of the composite part. As the density is uniform throughout the layer, it can be

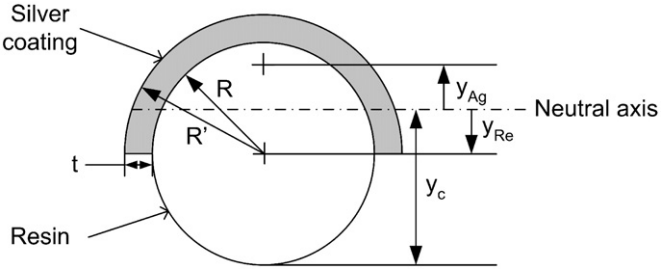

Fig. B1. Schematic of the cross-section of the beam.

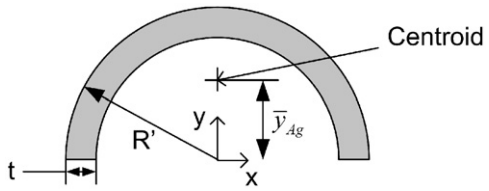

Fig. B2. Geometry of the silver coating.

shown that

$$\overline{y}_{Ag}=\frac{\int_{-R'}^{R'}\int_{0}^{\sqrt{R'^2-x^2}}y\,dydx-\int_{-R}^{R}\int_{0}^{\sqrt{R^2-x^2}}y\,dydx}{\int_{-R'}^{R'}\int_{0}^{\sqrt{R'^2-x^2}}dydx-\int_{-R}^{R}\int_{0}^{\sqrt{R^2-x^2}}dydx}$$

$$\overline{y}_{Ag}=\frac{4}{3\pi}\frac{R'^2+R'R+R^2}{R'+R} \tag{B3}$$

Collecting terms from the force balance gives

$$[2E_{Re}R^2+E_{Ag}(R'^2-R^2)]y_c=2E_{Re}R^3+E_{Ag}(R+\overline{y}_{Ag})(R'^2-R^2) \tag{B4}$$

Hence the location of the neutral axis can be given as

$$y_c=\frac{2E_{Re}R^3+E_{Ag}(R+\overline{y}_{Ag})(R'^2-R^2)}{[2E_{Re}R^2+E_{Ag}(R'^2-R^2)]} \tag{B5}$$

To calculate the flexural rigidity of the coated cantilever, it is necessary to know the second moments of area for each component. First consider the geometry of the resin component as shown in Fig. B1. It can be shown that the second moment of area of the cylinder about its centroid can be given as

$$I_{Re,CM}=\int_{-R}^{R}\int_{-\sqrt{R^2-x^2}}^{\sqrt{R^2-x^2}}y^2dydx=\frac{\pi R^4}{4} \tag{B6}$$

Similarly the second moment of area for the silver coating about its base can be shown to be

$$I_{Ag,CM}=\int_{-R'}^{R'}\int_{0}^{\sqrt{R'^2-x^2}}y^2dydx-\int_{-R}^{R}\int_{0}^{\sqrt{R^2-x^2}}y^2dydx=\frac{\pi(R'^4-R^4)}{8} \tag{B7}$$

Using the parallel axis theorem, $I=I_{CM}+Ay^2$, the second moment of area for each component about the neutral axis can be obtained thus

$$I_{Re}=\frac{\pi R^4}{4}+\pi R^2(R-y_c)^2 \tag{B8}$$

$$I_{Ag}=\frac{\pi(R'^4-R^4)}{8}+\frac{\pi}{2}(R'^2-R^2)(R+\overline{y}_{Ag}-y_c)^2 \tag{B9}$$

The total flexural rigidity for the coated cantilever can therefore be shown to be

$$EI=E_{Re}I_{Re}+E_{Ag}I_{Ag} \tag{B10}$$

It can be seen as a comparable situation that if the cantilever was coated on both sides that $\overline{y}_{Ag}$ would equal zero and y_c would equal R' if measured from the base of the coating. In this instance the expressions would simplify to

$$I_{Re}=\frac{\pi R^4}{4} \tag{B11}$$

$$I_{Ag}=\frac{\pi(R'^4-R^4)}{4} \tag{B12}$$

Appendix C. Conical cantilever theory

Using the method to fabricate the cylindrical cantilevers, it will also be possible to fabricate conical cantilevers (see Fig. C1).

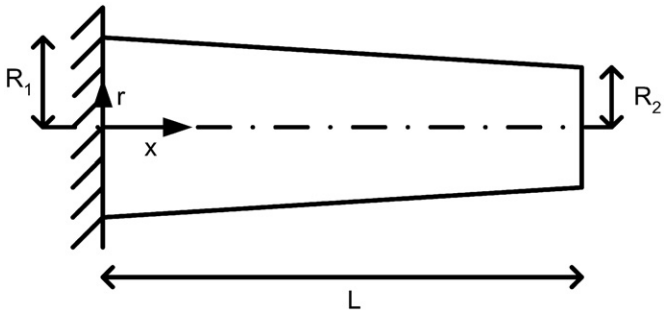

Fig. C1. The geometry of a conical cantilever.

Analysis of the conical cantilevers has the additional complication of having a non-uniform cross-section.

To keep the analysis simple, it will be assumed that the cantilever's radius to length ratio is sufficiently small so that shear effects and rotary inertia are negligible. In this instance the radius of the cantilever is given as

$$R(x)=\frac{dr}{dx}x+R_1=\left(\frac{R_2-R_1}{L}\right)x+R_1 \tag{C1}$$

This gives the second moment of area as

$$I(x)=\frac{\pi R^4}{4}=\frac{\pi}{4}\left[\left(\frac{R_2-R_1}{L}\right)x+R_1\right]^4 \tag{C2}$$

Using the standard Euler–Bernoulli beam equation

$$\frac{d^2}{dx^2}\left[EI(x)\frac{d^2u}{dx^2}\right]=0 \tag{C3}$$

Upon integrating

$$\frac{d}{dx}\left[EI(x)\frac{d^2u}{dx^2}\right]=P \tag{C4}$$

And again

$$EI(x)\frac{d^2u}{dx^2}=Px+C_1\Rightarrow\frac{d^2u}{dx^2}=\frac{Px}{EI(x)}+\frac{C_1}{EI(x)} \tag{C5}$$

And for a third time

$$\frac{du}{dx}=\frac{-2}{3\pi}\left\{\frac{3PLx(R_1-R_2)-R_1L^2P}{E(R_1-R_2)^2[(R_1-R_2)(x/L)-R_1]^3}\right\}-\frac{4}{3\pi}\left\{\frac{C_1L}{E(R_1-R_2)[(R_1-R_2)(x/L)-R_1]^3}\right\}+C_2 \tag{C6}$$

And finally

$$u=\frac{2L^2P}{3\pi E}\left\{\frac{3x(R_1-R_2)-2R_1L}{(R_1-R_2)^3[(R_1-R_2)(x/L)-R_1]^2}\right\}+\frac{2L^2}{3\pi E}\left\{\frac{C_1}{(R_1-R_2)^2[(R_1-R_2)(x/L)-R_1]^2}\right\}+C_2x+C_3 \tag{C7}$$

Given the boundary conditions at $x=0$, $u=(du/dx)=0$, Eqs. C22 and C23 become

$$\frac{2L^2}{3\pi E}C_1(R_1-R_2)+C_3\left[R_1^2(R_1-R_2)^3\right]=\frac{4L^3PR_1}{3\pi E} \tag{C8}$$

therefore

$$\frac{-4C_1L}{3\pi E}(R_1-R_2)+C_2\left[(-R_1)^3(R_1-R_2)^2\right]=\frac{-2L^2PR_1}{3\pi E} \tag{C9}$$

Similarly given this boundary condition at $x=L$, $EI(x)(d^2u/dx^2)=0$, the unknown constants can be seen to be

$$C_1=-PL \tag{C10}$$

Please cite this article as: D. Cheneler, et al., Ultramicroscopy (2011), doi:10.1016/j.ultramic.2011.03.009

$$C_2 = \frac{2PL^2}{3\pi E}\left[\frac{3R_1 - 2R_2}{{R_1}^3(R_1-R_2)^2}\right] \tag{C11}$$

$$C_3 = \frac{2PL^3}{3\pi E}\left[\frac{3R_1 - R_2}{{R_1}^2(R_1-R_2)^3}\right] \tag{C12}$$

Therefore the static deflection of a conical cantilever due to pure bending can therefore be shown to be

$$u(x) = \frac{2Px^2}{3\pi E}\left\{\frac{3R_1(x-L) - 2xR_2}{{R_1}^3[(R_1-R_2)(x/L)-R_1]^2}\right\} \tag{C13}$$

When $R_1 = R_2$, Eq. (C29) reduces down to

$$u(x) = \frac{2Px^2}{3\pi E{R_1}^4}(x-3L) \tag{C14}$$

As expected. Therefore, given Eq. (C29), the stiffness of a conical cantilever can be given as

$$K = \frac{3\pi E}{4L^3}R_2{R_1}^3 \tag{C15}$$

As above, the natural frequency of a conical cantilever can be approximated using Rayleigh's method. Neglecting shear deformation and rotary inertia effects, the angular frequency of a conical cantilever can be given as

$$\omega^2 = \frac{\int_0^L EI(x)(d^2u(x)/dx^2)^2 dx}{\int_0^L \rho A u(x)^2 dx} \tag{C16}$$

Given Eqs. C18 and C30 and the cross-sectional area given by $A = \pi[R_1 - (R_1 - R_2)(x/L)]^2$, the resonant frequency, in Hz, of a conical cantilever can be shown to be

$$f = \left[\frac{30E}{4\pi^2 L^4 \rho}\frac{R_1^3(R_1-R_2)^7}{R_2}\left((R_1-R_2)[18R_1^6 + 39R_1^5R_2 + 57R_1^4R_2^2 - 123R_1^3R_2^3 + 107R_1^2R_2^4 - 46R_1R_2^5 + 8R_2^6] + 60R_1^6R_2\ln\left(\frac{R_2}{R_1}\right)\right)^{-1}\right]^{1/2} \tag{C17}$$

References

[1] S. Schmid, P. Senn, C. Hierold, Sens. Actuators A 145–146 (2008) 442.
[2] R. Marie, S. Schmid, A. Johansson, L. Ejsing, M. Nordstroem, D. Haefliger, C.B.V. Christensen, A. Boisen, M. Dufva, Biosens. Bioelectron. 21 (2006) 1327.
[3] M.J. Madou, Fundamentals of Microfabrication, CRC-Press, London, 1998.
[4] S. Schmid, C. Hierold, J. Appl. Phys. 104 (2008) 093516.
[5] S. Mouaziz, G. Boero, R.S. Popovic, J. Brugger, J. Micromech. Syst. 15 (4) (2006) 890.
[6] M. Tenje, S. Keller, S. Dohn, Z.J. Davis, A. Boisen, Ultramicroscopy 110 (2010) 596.
[7] F. Battiston, J.-P. Ramseyer, H. Lang, M. Baller, C. Gerber, J. Gimzewski, E. Meyer, H.-J. Guntherodt, Sens. Actuators B 77 (2001) 122.
[8] B. Kim, D. Collard, M. Lagouge, F. Conseil, B. Legrand, L. Buchaillot, Transducers '03, in: Proceedings of 12th International Conference on Solid-State Sensors, Actuators and Microsystems, 2003, p. 1255.
[9] W.H. Song, A. Hierlemann, J. Lichtenberg, Transducers '05, in: Proceedings of 13th International Conference on Solid-State Sensors, Actuators and Microsystems, 2005, p. 2040.
[10] N. Kato, C.S. Park, T. Matsumoto, H. Kikuta, K. Iwata, in: Proceedings of SICE Annual Conference on Instrumentation, Control and Information Technology, 2004, p. 2656.
[11] S. Keller, D. Haefliger, A. Boisen, J. Vac. Sci. Technol. B 25 (6) (2007) 1903.
[12] R. Guerre, U. Dreschsler, D. Jubin, N. Despont, J. Micromech. Microeng. 18 (2008) 115013.
[13] M. Calleja, P. Rasmussen, A. Johansson, A. Boisen, Sens. Actuators MEMS 5116 (2003) 314.
[14] O. Ergeneman, M. Suter, G. Chatzipirpiridis, J. Zurcher, S. Graf, S. Pane, C. Herold, C. Nelson, in: Proceedings of International Symposium on Optomechatronic Technologies, 2009, p. 266.
[15] P.A. Rasmussen, J. Thaysen, O. Hansen, S.C. Eriksen, A. Boisen, Ultramicroscopy 97 (2003) 371.
[16] F.G. Bosco, E.-T. Hwu, S. Keller, A. Greve, A. Boisen, Microelectron. Eng. 87 (2010) 708.
[17] S. Keller, D. Haefliger, A. Boisen, J. Micromech. Microeng. 20 (2010) 1.
[18] F. Kuhner, R.A. Lugmaier, S. Mihatsch, H.E. Gaub, Rev. Sci. Instrum. 78 (2007) 075105.
[19] J. Bowen, D. Cheneler, D. Walliman, S.G. Arkless, Z. Zhang, M.C.L. Ward, M.J. Adams, Meas. Sci. Technol. 21 (2010) 115106.
[20] J.W. Choi, R.B. Wicker, S.H. Lee, K.H. Choi, I.D. Jung, C.S. Ha, I. Chung, J. Mater. Process. Technol. 209 (2009) 5494.
[21] J.M. Gere, S.P. Timoshenko, Mechanics of Materials, second ed., PWS Engineering, Boston, 1984.
[22] L. Majkut, J. Theor. Appl. Mech. 47 (1) (2009) 193.
[23] S.S. Rao, Mechanical Vibrations, fourth ed., Prentice Hall, 2003.
[24] J.R. Hutchinson, J. Appl. Mech. 68 (1) (2001) 87.
[25] C.M. Wang, J. Eng. Mech. 121 (6) (1995) 763.
[26] P. Hess, App. Surf. Sci. 106 (1996) 433.
[27] M. Puttock, NSLT Technical Paper 25, 1969, p. 1.
[28] F. Sansoz, T. Gang, Ultramicroscopy 111 (2010) 11.
[29] J.J. Roa, E. Jiménez-Piqué, X.G. Capdevila, M. Segarra, J. Euro. Ceram. Soc 30 (2010) 1477.
[30] T.R. Albrecht, S. Akamine, T.E. Carver, C.F. Quate, J. Vac. Sci. Technol. A 8 (1990) 3386.
[31] C. Beuret, T. Akiyama, U. Staufer, N.F. de Rooij, P. Niedermann, W. Hänni, Appl. Phys. Lett. 76 (2000) 1621.
[32] W.A. Ducker, T.J. Senden, R.M. Pashley, Nature 353 (1991) 239.
[33] W.A. Ducker, T.J. Senden, R.M. Pashley, Langmuir 8 (1992) 1831.